

Doublon Production in Correlated Materials by Multiple Ion Impacts

Lotte Borkowski, Niclas Schlünzen, Jan-Philip Joost,* Franziska Reiser, and Michael Bonitz

Recently, it was demonstrated that ions impacting a correlated finite graphene-type honeycomb cluster can excite strong nonequilibrium states. In particular, this can lead to an enhanced population of bound pairs of electrons with opposite spin—doublons—where the doublon number can be increased further via multiple ion impacts. These predictions were made based on nonequilibrium Green functions (NEGF) simulations allowing for a time-dependent non-perturbative study of the energy loss of charged particles penetrating a strongly correlated system. Herein, these simulations are extended to larger clusters and longer simulation times, utilizing the recently developed G1–G2 scheme, which allows for a dramatic speedup of NEGF simulations. Furthermore, the dependence of the energy and doublon number on the time interval between ion impacts and on the impact point is investigated.

1. Introduction

The interaction of charged particles with matter is of high relevance for many areas of physics and astrophysics. Properties such as the stopping power or stopping range of projectiles in matter allow one to analyze their energy spectrum. On the other hand, the energy loss of charged particles in matter is a sensitive tool to diagnose the electronic properties of the material. In soft collisions of heavy charged particles, such as ions, with a solid, typically the electrostatic force, that is, the Coulomb interaction, has the largest impact, leading to excitation and ionization of electrons in the target material and, thus, to the loss of kinetic energy of the projectile.^[1] For nonrelativistic projectile velocities of the order of or larger than the Fermi velocity ($\sim 10^6 \text{ m s}^{-1}$ in metals), theoretical approaches based on

scattering theory^[2] or on the linear response functions of the uniform electron gas^[3] provide an accurate description of the energy transferred during the collision process. However, they neglect the precise atomic composition of the target, electronic correlations, and nonlinear effects.^[4,5]


In the same velocity regime, recent theoretical progress is due to time-dependent density functional theory (TDDFT), which has been applied to describe the slowing down of charged particles in a variety of solids, including metals,^[6–8] semimetals,^[9,10] and clusters,^[11,12] narrow-bandgap semiconductors,^[13] insulators,^[14,15] and monolayer systems such as graphene (see, for example, Ref. [16]). Taking into account primarily the excitation of valence electrons, these simulations

yield satisfactory results for the electronic stopping power (the transfer of energy to the electronic degrees of freedom per unit length traveled by the projectile) and work for a wide range of impact energies. In contrast, a rather general tool to determine the stopping power of energetic ions in matter is provided by “The Stopping and Range of Ions in Matter” (SRIM) code,^[17] which uses the binary collision approximation in combination with averaging over a large range of experimental situations, and data being available for many materials and gaseous targets. At the same time, linear response, TDDFT, and SRIM have difficulties in accounting for strong electron–electron correlations, which are crucial, for example, in transition metal oxides^[18] or certain organic materials.^[19] In addition, we note that SRIM and linear response theory do not account for time-dependent changes in the target during the collision process, which limits their applicability.

For this reason, we have developed an alternative approach to the stopping power that is based on nonequilibrium Green functions (NEGF).^[20–23] Direct numerical solutions for the NEGF have been pioneered by Danielewicz^[24] and further developed by Koehler et al.,^[25,26] Bonitz et al.,^[27–29] and others. Direct NEGF solutions have recently successfully been applied to inhomogeneous systems by van Leeuwen et al.^[30–33] More recently, also strongly correlated lattice systems came into the focus of NEGF simulations, for example, Refs. [34–37].

The NEGF approach allows one to systematically include electron–electron correlations via a time-dependent many-body self-energy. A particular advantage of the NEGF approach is that it is not limited to either weak or strong coupling and that it is particularly well suited to study finite-sized clusters of any geometry and spatially inhomogeneous systems.

L. Borkowski, N. Schlünzen, J.-P. Joost, F. Reiser, M. Bonitz
Institut für Theoretische Physik und Astrophysik
Christian-Albrechts-Universität zu Kiel
Leibnizstrasse 15, 24098 Kiel, Germany
E-mail: joost@theo-physik.uni-kiel.de

 The ORCID identification number(s) for the author(s) of this article can be found under <https://doi.org/10.1002/pssb.202100511>.

© 2022 The Authors. physica status solidi (b) basic solid state physics published by Wiley-VCH GmbH. This is an open access article under the terms of the Creative Commons Attribution-NonCommercial License, which permits use, distribution and reproduction in any medium, provided the original work is properly cited and is not used for commercial purposes.

DOI: 10.1002/pssb.202100511

Recently, NEGF simulations coupled to an Ehrenfest dynamics of the projectile were developed,^[38] and good agreement with TDDFT and SRIM simulations was established. A particularly interesting result of NEGF simulations in the low velocity range was the prediction of a nontrivial electronic correlation effect: the formation of doublons, that is, bound pairs of electrons with opposite spin, as a result of ion impact. In a recent Letter,^[39] it was demonstrated that the doublon number can be further increased if the material is hit by multiple ions. This issue was further explored in Refs. [40,41]. Another important issue during the impact of ions on solid targets is the possible transfer of charge to the ion (neutralization), which has been studied in a number of experiments, for example, Refs. [42,43]. A first attempt to extend the NEGF-Ehrenfest approach to include charge exchange processes has been made in Ref. [44].

However, the NEGF approach is computationally very demanding. While in recent years efficient numerical schemes have been developed to solve the underlying Keldysh–Kadanoff–Baym equations (KBE),^[22,37,45–50] the solution is hampered by a cubic scaling of the CPU time with the number of time steps N_t . This scaling can be reduced to quadratic by applying the generalized Kadanoff–Baym ansatz (HF-GKBA)^[51] which, in recent years, was applied to finite correlated systems, including Hubbard clusters,^[37] graphene nanoflakes,^[52] as well as atoms and molecules.^[50,53] Recently, we showed that even linear scaling can be achieved if the HF-GKBA is rewritten as a coupled system of time-local equations for the one- and two-particle Green function, which was called “G1–G2 scheme”^[54] and has already found a variety of applications, for example, Refs. [55,56].

In the present paper, we take advantage of the speedup provided by the G1–G2 scheme to significantly extend the previous ion stopping simulations for the case of multiple impacts of Ref. [39]. As in that work, we concentrate on generic finite hexagonal graphene-type monolayer clusters, but we study significantly larger clusters of up to 96 sites, and extend the simulation duration. Moreover, we study how the excitation by the ion propagates through the cluster.

In addition, we vary the time interval between successive ion impacts as well as the impact point and investigate how this influences the energy of the electrons and the doublon production. For short time intervals between impacts, we are able to analyze nonadiabatic response phenomena where the effect of two projectiles does not simply add up because the cluster is driven far from equilibrium. In addition to the long-range Coulomb interaction between cluster electrons and projectile, we also consider a simpler model, where the effect of the projectile is mimicked by a predefined Gaussian variation of the lattice potential. This scenario was also introduced in Ref. [39] and is of interest not only for strongly correlated materials, but also for cold atoms in an optical lattice, where it can easily be realized experimentally.

The paper is organized as follows. In Section 2, we define the model Hamiltonian and introduce our NEGF approach as well as the G1–G2 scheme. In Section 3, we present the simulation results. We conclude the paper with a summary and discussion in Section 4, outlining possible future work.

2. Theory

2.1. Hubbard Model for Finite Graphene-Type Honeycomb Clusters

To study the stopping dynamics of a classical charged particle which passes through a correlated system, we consider a finite lattice of electrons described by a single-band Fermi–Hubbard model and compute the energy exchange between projectile and cluster during the collision process. Details of the model are described in Ref. [38]. Here, we only summarize the main points. The lattice as a whole is electrically neutral, in that, the electronic charges are compensated by corresponding opposite charges located at the site coordinates \mathbf{R}_i . The energy exchange occurs via the Coulomb potential between the projectile, the fixed background charges, and the target electrons, which are initially in equilibrium. As the projectile, we consider positively charged ions. When they approach the lattice, they induce a confinement potential to the electrons, which initiates a nonequilibrium electron dynamics. As a target, we consider circular honeycomb clusters in the xy -plane with a finite number of honeycombs and a total of L sites, see **Figure 1** for an illustration. We focus on a half-filled system in the paramagnetic phase and use a lattice spacing of $a_0 = 1.42$ Å, which corresponds to the carbon–carbon bond length in graphene.^[57] Using a nearest-neighbor hopping J and an on-site Hubbard repulsion U (which we consider time dependent to account for adiabatic-switching procedures^[23]), the Hamiltonian for the lattice electrons is then given by

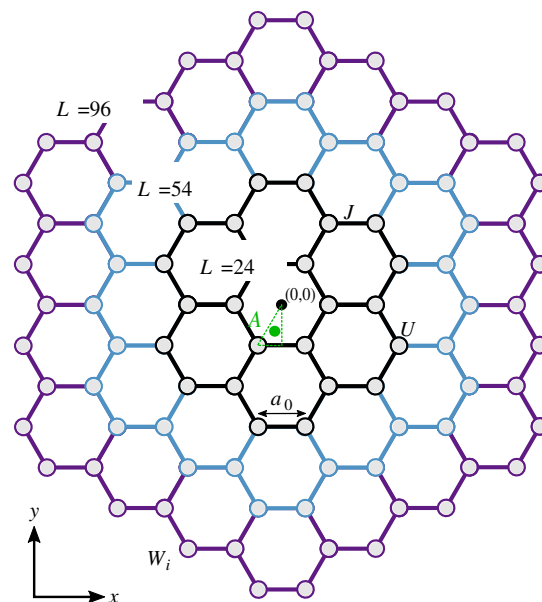


Figure 1. Lattice structure of circular honeycomb clusters with $L = 24$ (black), 54 (blue), and 96 (purple) sites. The green point $A = \left(-\frac{1}{6}a_0, -\frac{\sqrt{3}}{3}a_0, 0\right)$ indicates the position where the projectile hits the lattice plane. Furthermore, $a_0 = 1.42$ Å denotes the lattice spacing, $J = 2.8$ eV is the nearest-neighbor hopping, U the on-site interaction, and W_i is the time-dependent local energy produced by the projectile, cf. Equation (2).

$$H_e(t) = -J \sum_{(i,j),\sigma} \hat{c}_{i\sigma}^\dagger \hat{c}_{j\sigma} + U(t) \sum_i \hat{n}_i^\uparrow \hat{n}_i^\downarrow + \sum_{i,\sigma} W_i(t) \hat{c}_{i\sigma}^\dagger \hat{c}_{i\sigma} \quad (1)$$

where the operator $\hat{c}_{i\sigma}^\dagger$ ($\hat{c}_{i\sigma}$) creates (annihilates) an electron with spin σ on site i . Further, $\hat{n}_{i\sigma} = \hat{c}_{i\sigma}^\dagger \hat{c}_{i\sigma}$ and W_i denote the electron density operator and the external potential produced by the projectile, respectively. As a comment we note that this Hamiltonian has been used broadly to study graphene structures.^[58–60]

For convenience, we measure J and U in electron volts, define U/J as the interaction strength for the electrons, and use $t_0 = \hbar/J$ as the unit of time. Unless otherwise stated, we use $J = 2.8$ eV which is typical for graphene^[61] and corresponds to $t_0 = 0.235$ fs. As was shown in Ref. [39], the effect of doublon formation by ion impact can be reliably induced for an electronic coupling of $U = 4J$. Therefore, here, we choose the same value, to investigate in more detail the prospects of doublon formation. While this value is higher than in graphene, similar values of the coupling parameter are observed in quantum-confined finite graphene nanostructures (e.g., nanoribbons)^[62,63] or in monolayers of transition metal dichalcogenides.

To analyze the influence of the 2D geometry of the presented honeycomb lattices, we also consider a 1D Hubbard chain as a reference model in some calculations. This system is also described by the Hamiltonian of Equation (1). We mention that effective 1D systems can be realized in optical-lattice experiments with ultracold atoms (see, e.g., Ref. [64]).

2.2. Incident-Ion Potential

We consider two different models to describe the time-dependent potential induced by the energetic ions. In the first scenario, we compute the classical **Coulomb** potential of incident ions of charge Z_p ,

$$W_i(t) = -\frac{e^2}{4\pi\epsilon_0} \frac{Z_p}{|\mathbf{r}_p(t) - \mathbf{R}_i|} \quad (2)$$

where $\mathbf{r}_p(t)$ denotes the time-dependent position of the projectile, $-e$ is the electron charge, and ϵ_0 is the vacuum permittivity. Throughout this paper, we consider the excitation by energetic protons, that is, $Z_p = 1$. In analogy to previous studies,^[38,41] we set the initial position of the incident ion to $\mathbf{r}_{p,0} = \left(-\frac{1}{6}a_0, -\frac{\sqrt{3}}{3}a_0, -z\right)$, see the centroid point of the green dashed triangle in Figure 1. These coordinates have been found to give similar stopping results for the highly symmetric honeycomb lattice compared to calculations, where one averages over many different collision sites. The influence of the impact point will be studied separately in Section 3.6. Furthermore, the initial z -position is chosen such that the measured energy transfer becomes independent of the initial conditions (typically $z \gtrsim 10a_0$).

The dependence of the energy exchange on the impact velocity was investigated in detail in Refs. [38,39]. Here, we are interested in the response of the target electrons to a varying number of projectiles. To this end, we fix the ion velocity to a value $v_{p,0} = 3a_0/t_0 \approx 1.8 \times 10^6$ m s⁻¹ in the z -direction, cf. Equation (21). This is a comparatively large value, near the maximum of the

stopping curve. The corresponding kinetic energy of the projectile is much larger than the energy exchanged with the target. Therefore, a self-consistent solution of Newton's equation for the projectile can be avoided for all cases considered in this paper.

It is often useful to simplify the general Coulomb potential to investigate local effects induced by the excitation. For such applications, a short-ranged localized potential that excites a specific lattice site provides a reasonable approximation.^[39] We will use a **Gaussian**,

$$W_i(t) = -W_0 \delta_{i,i_0} \exp\left(-\frac{t^2}{2\tau^2}\right) \quad (3)$$

with the amplitude W_0 , the excited lattice site i_0 (which we choose on the innermost honeycomb ring), and the interaction duration $\tau > 0$. This model is closely related to the full Coulomb model where τ is inversely proportional to the ion velocity, while W_0 is proportional to the charge of the ion.^[39] For the best correspondence between the two models, we use $\tau = 0.5\hbar/J$ and $W_0 = 8J$. We note that the Gaussian potential is also of practical relevance for experiments with ultracold atoms in optical lattices and allows one to simulate ion stopping (for a recent overview, see Ref. [65]).

2.3. Nonequilibrium Green Functions

We compute the correlated time evolution of the lattice electrons, using an NEGF approach, as described in Ref. [38]. The central quantity is the one-particle Green function (here and in the following, we only give the spin-up components (\uparrow) explicitly, the spin-down components follow from replacing $\uparrow \leftrightarrow \downarrow$)

$$G_{ij}^\uparrow(t, t') = -\frac{i}{\hbar} \left\langle T_C \hat{c}_{i\uparrow}(t) \hat{c}_{j\uparrow}^\dagger(t') \right\rangle \quad (4)$$

which is defined as an ensemble average on the Keldysh time contour \mathcal{C} ,^[66] and T_C denotes the contour time-ordering operator. The equations of motion of the greater and lesser components of the one-particle NEGF (Equation (4))

$$\begin{aligned} G_{ij}^{>\uparrow}(t, t') &= -\frac{i}{\hbar} \left\langle \hat{c}_{i\uparrow}(t) \hat{c}_{j\uparrow}^\dagger(t') \right\rangle \\ G_{ij}^{<\uparrow}(t, t') &= \frac{i}{\hbar} \left\langle \hat{c}_{j\uparrow}^\dagger(t') \hat{c}_{i\uparrow}(t) \right\rangle \end{aligned} \quad (5)$$

are the two-time KBE,^[20,21,46]

$$\begin{aligned} \sum_k [i\hbar \partial_t \delta_{ik} - h_{ik}^{\text{HF},\uparrow}(t)] G_{kj}^{>\uparrow}(t, t') &= \delta_C(t, t') \delta_{ij} \\ &+ \sum_k \left\{ \int_C ds \Sigma_{ik}^\uparrow(t, s) G_{kj}^\uparrow(s, t') \right\}^\cong \end{aligned} \quad (6)$$

Here, δ_C denotes the delta function on the contour, and $h_{ij}^{\text{HF},\uparrow}(t)$ is the time-dependent effective one-particle Hamiltonian, which explicitly includes the Hartree contribution to the electron–electron interaction,

$$h_{ij}^{\text{HF},\uparrow}(t) = -\underbrace{J\delta_{ij}}_{=J_{ij}} + [W_i(t) - i\hbar U(t)G_{ii}^{<,\downarrow}(t)]\delta_{ij} \quad (7)$$

On the right-hand side of Equation (6), the contour integral defines the memory kernel of the KBE, in which $\Sigma_{ij}^{\uparrow}(t, t')$ denotes the correlation part of the self-energy (i.e., the mean-field part is excluded as it is contained in Equation (7)). Systematic expressions for the self-energy can be constructed by many-body perturbation theory, for example, using diagram techniques.^[21,67] Below, we treat the self-energy Σ in two approximations, which conserve particle number, momentum, and energy. (i) Mean-field approximation (time-dependent Hartree–Fock); here correlation effects are neglected. (ii) Second-order Born approximation (SOA),

$$\Sigma_{ij}^{<,\uparrow}(t, t') = -(i\hbar)^2 U(t)U(t') \times G_{ij}^{<,\uparrow}(t, t')G_{ij}^{<,\downarrow}(t, t')G_{ji}^{<,\downarrow}(t', t) \quad (8)$$

which includes all irreducible diagrams of second order in the interaction U . We note that the SOA self-energy is a perturbation theory result and, therefore, becomes less accurate when U increases. In the context of ion-impact simulations on finite graphene-type honeycomb clusters, the accuracy of the SOA scheme has been validated in Ref. [39].

A detailed recent overview on different self-energy approximations and their accuracy can be found in the review by Schlünzen et al.^[23]

2.4. G1–G2 Scheme

The advantage of NEGF simulations is that they allow one to accurately capture electronic correlation effects. At the same time, NEGF simulations are computationally expensive because the CPU time scales cubically with the number of time steps, $\approx N_t^3$. In the recent publications, Refs. [54,68], it was demonstrated that the KBE in combination with the HF-GKBA^[37,51] can be solved highly efficiently within a set of time-local differential equations, bringing the CPU time scaling down to N_t^1 . In this description, the equation of motion for the time-diagonal single-particle Green function becomes^[68]

$$i\hbar \frac{d}{dt} G_{ij}^{<,\uparrow}(t) = [h^{\text{HF},\uparrow}(t), G_{ij}^{<,\uparrow}(t)]_{ij} + [I + I^\dagger]_{ij}^\uparrow(t) \quad (9)$$

The information of the self-energy is included in the correlation part of time-diagonal two-particle Green function \mathcal{G} as

$$I_{ij}^\uparrow(t) = \sum_k \int_{t_0}^t d\bar{t} [\Sigma_{ik}^{>,\uparrow}(t, \bar{t})G_{kj}^{<,\downarrow}(\bar{t}, t) - \Sigma_{ik}^{<,\uparrow}(t, \bar{t})G_{kj}^{>,\uparrow}(\bar{t}, t)] \\ = -i\hbar U(t)\mathcal{G}_{iji}^{\uparrow\uparrow\downarrow}(t) \quad (10)$$

The correlation function \mathcal{G} obeys its own equation of motion, which, for the SOA self-energy (cf. Equation (8)), attains the form

$$i\hbar \frac{d}{dt} \mathcal{G}_{ijkl}^{\uparrow\uparrow\downarrow}(t) - [h_{i\downarrow}^{(2),\text{HF}}, \mathcal{G}_{ijkl}^{\uparrow\uparrow\downarrow}]_{ijkl}(t) = \Psi_{ijkl}^{\uparrow\uparrow\downarrow}(t), \quad (11)$$

with the two-particle Hartree–Fock (HF) Hamiltonian

$$h_{ijkl}^{(2),\text{HF}}(t) = \delta_{jl}h_{ik}^{\text{HF},\uparrow}(t) + \delta_{ik}h_{jl}^{\text{HF},\downarrow}(t) \quad (12)$$

and the two-particle source term

$$\Psi_{ijkl}^{\uparrow\uparrow\downarrow}(t) = (i\hbar)^2 U(t) \sum_p [G_{ip}^{>,\uparrow}(t)G_{jp}^{>,\downarrow}(t)G_{pk}^{<,\uparrow}(t)G_{pl}^{<,\downarrow}(t) \\ - G_{ip}^{<,\uparrow}(t)G_{jp}^{<,\downarrow}(t)G_{pk}^{>,\uparrow}(t)G_{pl}^{>,\downarrow}(t)] \quad (13)$$

The coupled equations, Equation (9) and (11), are called the G1–G2 scheme and are closely related to the density-operator formalism.^[69] For this work, the equations are propagated with a fourth-order Runge–Kutta integration scheme. From the resulting $G^{<}$ and \mathcal{G} , we have direct access to the observables of interest, namely the site-resolved densities and double occupation:

$$n_{ij}(t) = n_{ij}^\uparrow(t) + n_{ij}^\downarrow(t) = -i\hbar [G_{ij}^{<,\uparrow}(t) + G_{ij}^{<,\downarrow}(t)] \quad (14)$$

$$d_i(t) = n_{ii}^\uparrow(t)n_{ii}^\downarrow(t) + (i\hbar)^2 \mathcal{G}_{iii}^{\uparrow\uparrow\downarrow}(t) \quad (15)$$

where d_i consists of a mean-field (first term) and a correlation contribution (second term). We will also compute the cluster-averaged doublon number,

$$d_{\text{av}}(t) = \frac{1}{L} \sum_i d_i(t) \quad (16)$$

Another important observable is the total energy of the target,

$$E(t) = E_{\text{kin}}(t) + E_{\text{pot}}(t) + E_{\text{int}}(t) \quad (17)$$

comprising the kinetic, potential, and interaction energy contributions,

$$E_{\text{kin}}(t) = -J \sum_{ij} \delta_{<i,j>} n_{ji}(t) \quad (18)$$

$$E_{\text{pot}}(t) = \sum_i W_i(t) n_{ii}(t) \quad (19)$$

$$E_{\text{int}}(t) = U(t) \sum_i d_i(t) \quad (20)$$

3. Numerical Results

3.1. Benchmarks against Previous HF-GKBA Simulations

When an ion penetrates through the target, the electric potential forces the lattice electrons to accumulate near the impact point. For sufficiently fast projectiles, this corresponds to a nonadiabatic excitation, leading to an overall energy gain for the cluster electrons. This behavior is shown in **Figure 2**, which gives a general overview of the impact dynamics. The figure depicts the total time evolution of the total energy of the target averaged over the number of lattice sites for the case of a single projectile impact. We compare two finite hexagonal systems containing 24 and 96 sites, respectively. Further, we study the influence of the projectile models presented in Section 2.2. Finally, the effect of

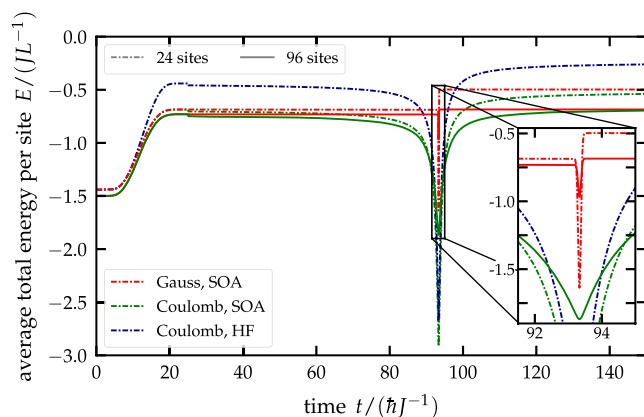


Figure 2. Average total energy per site of two different lattice sizes, $L = 24$ (dash-dotted lines) and $L = 96$ (solid lines) for a single excitation of the system around $t = 93t_0$ with $t_0 \approx 0.235$ fs. The three different colors denote different potentials and self energies. For the blue and green curves, the Coulomb potential is used to mimic the projectile impact with either time-dependent Hartree–Fock (HF, blue) or SOA (green) as self-energy approximation. The red curves correspond to an impact mimicked by the Gaussian potential, Equation (3), in SOA calculations.

the electron–electron interaction in the target is analyzed by comparing results for the HF and SOA self-energies.

Let us briefly summarize what we observe in Figure 2. First, one clearly distinguishes four phases. The first, from $t = 0$ to $t \approx 25t_0$, depicts the adiabatic switch-on (AS) of correlations, which allows us to start the simulations from an uncorrelated initial state. Adiabatic switching is a well established procedure to generate correlated initial states which has been used both in two-time simulations,^[21,23,67] and HF-GKBA calculations.^[67,70,71] Here, we apply the same method within the formally equivalent G1–G2 scheme. We performed a detailed analysis of the optimal parameter choice to ensure converged characteristic observables, such as the density matrix. For the present simulations we found that a preparation time of $25t_0$ is sufficient in order to reliably generate a stationary ground state for all considered systems. More details will be presented elsewhere.^[72] Thus, around $t = 25t_0$, a correlated initial state is achieved which is crucial for a self-consistent dynamical treatment of the projectile–target interaction. Note that the small kink in the energy at $t = 25t_0$ is due to the switch-on of the electron–ion interaction, which is very small but finite for the chosen initial position of the ion. The second and third phases describe the ion approaching and penetrating the honeycomb flake around $t = 93t_0$. Finally, the fourth phase describes the departure of the ion after traversal of the target. The increased total energy of the lattice corresponds to the projectile's energy loss, which we cannot measure directly within our description.

The amount of transferred energy depends on the electronic correlations in the target and on the theoretical model: the energy gain of the target is higher for HF results than for SOA, in agreement with earlier studies.^[38] If the lattice size is increased, the transferred energy is distributed among a larger number of lattice electrons. As a consequence, the energy gain per lattice site is reduced (compare the dashed and full red lines in the inset).

Regarding the models of the ionic potential, we observe that—with a suitable choice of parameters—the Gaussian model reproduces the energy gain of the lattice very well (compare the initial and final energies of the red and green curves in phases 2 and 4). However, there are drastic differences during the impact phase. Here, the full long-range Coulomb model predicts significantly larger intermediate energy exchange between projectile and target electrons. This is due to the long range of the Coulomb potential, that affects a larger number of lattice charges. This effect is even more pronounced in the case of multiple ion impacts (see Section 3.2.). Finally, the increased magnitude of the energy exchange is also important for a proper analysis of the details of the excitation mechanism, which involves two-electron excitations and doublon formation.^[39,40]

3.2. Multiple Ion Impacts: Gauss Model versus Coulomb Interaction

When increasing the number of projectiles impacting the honeycomb cluster, a general total energy gain in the lattice can be observed as shown in Figure 3a. It depicts the total energy dynamics of the smallest lattice introduced in Figure 1 containing $L = 24$ sites. In total, this lattice was excited 20 times ($N_x = 20$) for the Gaussian (red) and the Coulomb (green) potential respectively. Thereby, every peak corresponds to a projectile impact, while the different depths of the peaks can be attributed to the disparate shape and range of the potentials. Both curves describe a proton with an initial distance and velocity of

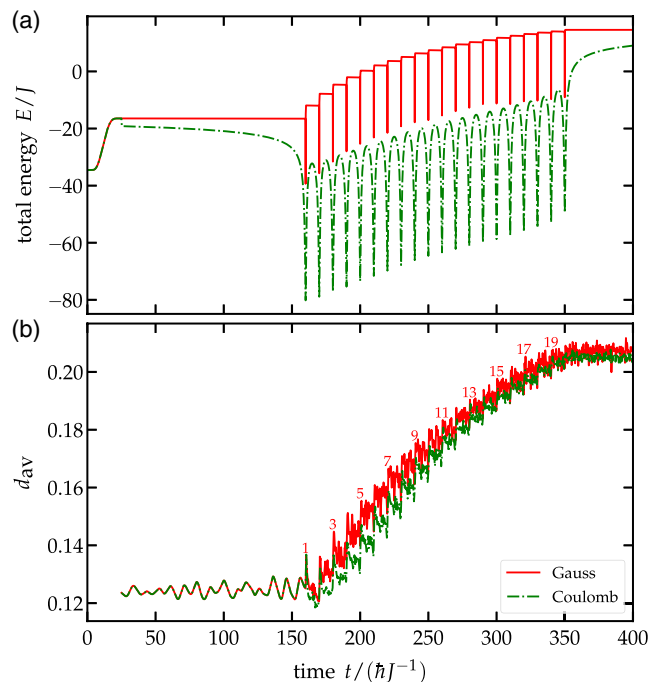


Figure 3. a) Total energy increase of the lattice containing $L = 24$ sites (cf. Figure 1) induced by 20 projectile impacts. Comparison of the Gaussian model (red) and the Coulomb interaction potential (green). b) Cluster-averaged doublon number. Number of the impacting ions is denoted in the figure. The model details are described in Section 2.2.

$$\mathbf{r}_{p,0} = - \begin{pmatrix} 1 \\ \frac{\sqrt{3}}{3} \\ 300 \end{pmatrix} a_0, \quad \mathbf{v}_{p,0} = \begin{pmatrix} 0 \\ 0 \\ 3 \end{pmatrix} \frac{a_0}{t_0} \quad (21)$$

with $t_0 = \frac{\hbar}{J} \approx 0.235$ fs and $v_{p,0} \approx 1.813 \cdot 10^6$ m s⁻¹.

The coordinate $\mathbf{r}_{p,0}$ corresponds to the green point A in Figure 1 and was used as impact point for the Coulomb potential unless stated otherwise. In contrast, the Gaussian potential is directly applied to one of the innermost lattice sites.

Figure 3a shows an initial increase of the total energy until $t = 25t_0$, which is due to the AS of electronic correlations in the solid.^[23] After the AS, the respective time-dependent interaction potential with the projectile is turned on. The small kink in the green curve for the total energy at $t = 25t_0$ is due to the long range of the Coulomb interaction. This kink could be easily eliminated by a different procedure of turning on the projectile–electron interaction, but this would require additional computational cost. When the projectile approaches the cluster plane, the total electron energy rapidly decreases, and then increases again as the ion leaves. With each new ion this behavior occurs again, in agreement with Figure 2. Next, we focus on the time evolution of the double occupation, Equation (16), which is plotted in Figure 3b. We observe that, through multiple periodical excitations, the overall double occupation in the 2D finite cluster can be significantly increased regardless of the potential chosen to mimic the projectile. In the figure, every second excitation is numbered. The instant when an ion passes through the lattice plane is clearly visible from the peaks of d_{av} . If the number of impacts were to be increased further, both curves are expected to eventually reach $d_{av} = 0.25$, the value in an uncorrelated system at half filling, cf. Equation (15). This is also confirmed by the time evolution of the correlation energy, which steadily decreases with increasing number of excitations.

We now consider a larger system with $L = 96$ sites that is exposed to an increased number of excitations, $N_x = 40$, the results are presented in Figure 4.

While the overall behavior (cf. Figure 4a) is the same as in Figure 3, here we observe larger deviations in d_{av} between the Gaussian and Coulomb models, cf. Figure 4b. The reason is the local excitation of a single lattice site, in case of the Gaussian model. With increase of the cluster size, a growing number of sites remains unaffected, in contrast to the long-range Coulomb model.

A novel observation is the slight decrease of the average double occupation during the first few ion impacts. This is observed for both potentials, even though the total energy shows different behaviors in the two cases. This effect will be further investigated in the following sections.

3.3. Dependence of Doublon Creation on the Cluster Size

In the following, the effect of the system size on the double occupation dynamics is investigated in more detail. Figure 5 shows Coulomb results for lattices of three sizes, $L = 24, 54, 96$. While the overall trend of an increase of the doublon number is observed for all systems, for a larger lattice the increase is slower.

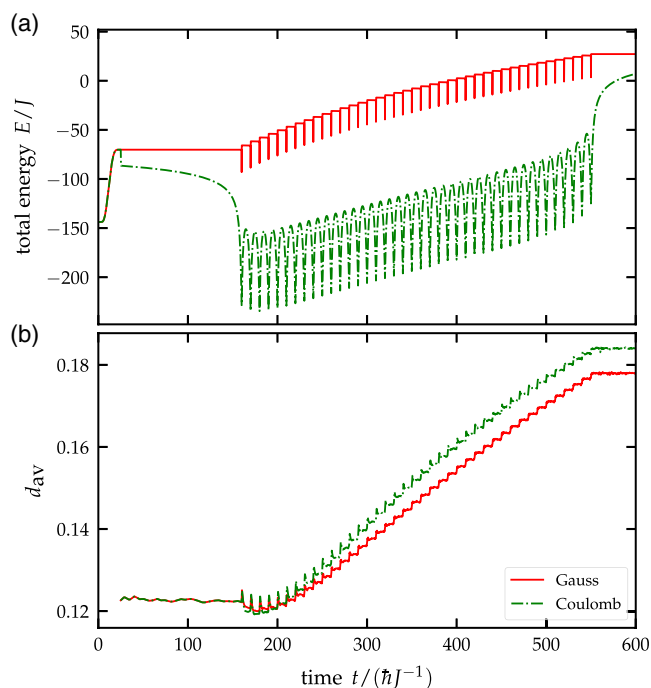


Figure 4. a) Total energy and b) corresponding double occupation increase of the $L = 96$ lattice induced by 40 projectile impacts modeled by a Gaussian potential (red) as well as a Coulomb potential (green). Same input parameters as in Figure 3.

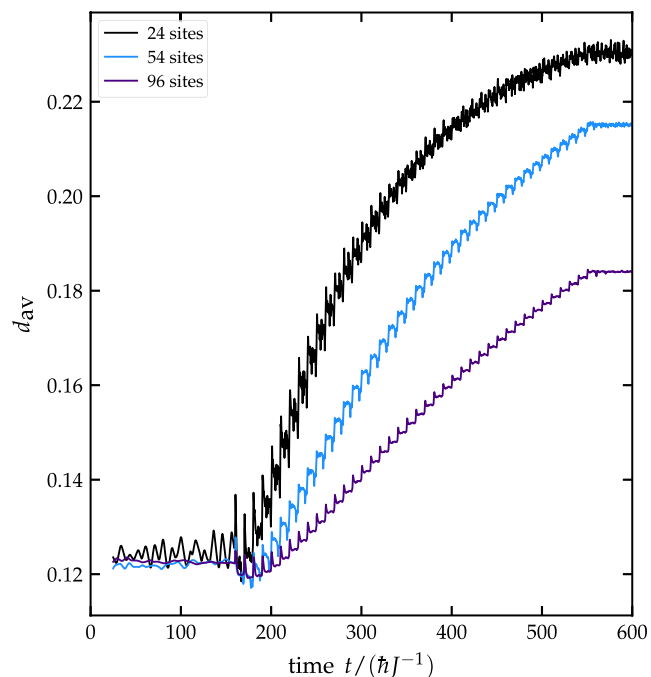


Figure 5. Cluster-averaged double occupation increase through $N_x = 40$ Coulomb excitations for three honeycomb lattice sizes: $L = 24$ (black), $L = 54$ (blue), and $L = 96$ (purple). Same parameters as in Figure 3.

The larger the lattice, the more excitations are needed to reach a specific value for d_{av} , since the projectile energy is shared between a growing number of electrons, in agreement with the observations of Balzer et al.^[39] Moreover, for the same reason, the peak height resulting from individual impacts and the noise in between two consecutive excitations is reduced when the lattice grows. Another interesting observation is that the broad global minimum mentioned in the previous section seems to widen for growing cluster sizes. Thus, more excitations are needed to escape that minimum.

We now investigate the asymptotic value of the mean double occupation,

$$d_{av}^{\infty} = \lim_{t \rightarrow \infty} \frac{1}{\Delta t} \int_t^{t+\Delta t} \bar{d} \bar{d}_{av}(\bar{t}) \quad (22)$$

which is computed after each excitation. This quantity was analyzed in Ref. [39] for moderate size 1D and 2D honeycomb clusters using HF-GKBA simulations. We now apply the G1–G2 scheme which allows us to extend the analysis to twice as large systems and to larger numbers of excitations. To compare with Ref. [39], we employ the Gaussian potential and use the same input parameters. Overall, the larger systems monotonically continue the trends of the previous results, which is shown in **Figure 6**. We also find that the G1–G2 scheme yields very good agreement with the previous HF-GKBA results; a more detailed comparisons can be found in Ref. [73].

Moreover, the previously addressed broad global minimum is observable in the bottom panel at $L = 96$, as the curve of the first excitation yields a higher average double occupation than the next, corresponding to $N_x = 4$. This minimum is not visible for the 1D setup. Furthermore, we observe that the 2D setup features a much greater initial level of the average double occupation than the 1D one.

The effect of the dimensionality is explored more in detail in **Figure 7**, where we compare 1D and 2D clusters containing the

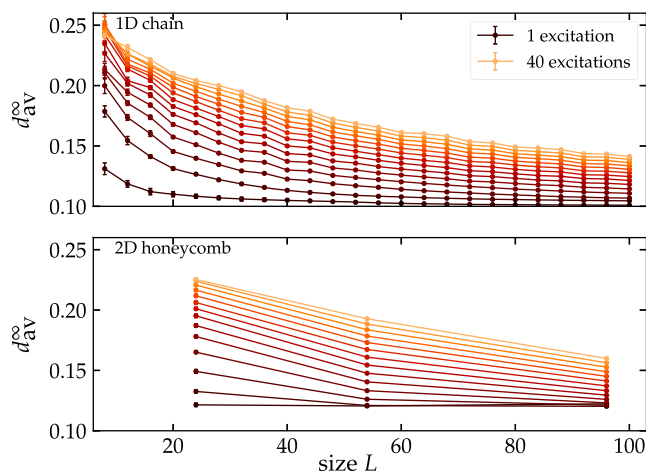


Figure 6. Asymptotic value of the mean double occupation for 1D chains consisting of up to $L = 100$ sites (top panel) and 2D honeycomb clusters with a maximum of $L = 96$ sites (bottom panel). All systems are excited between 1 (black curve) and 40 times (light orange) and every third excitation is plotted as a curve. The Gaussian model is used, and the initial values were chosen the same as in Ref. [39].

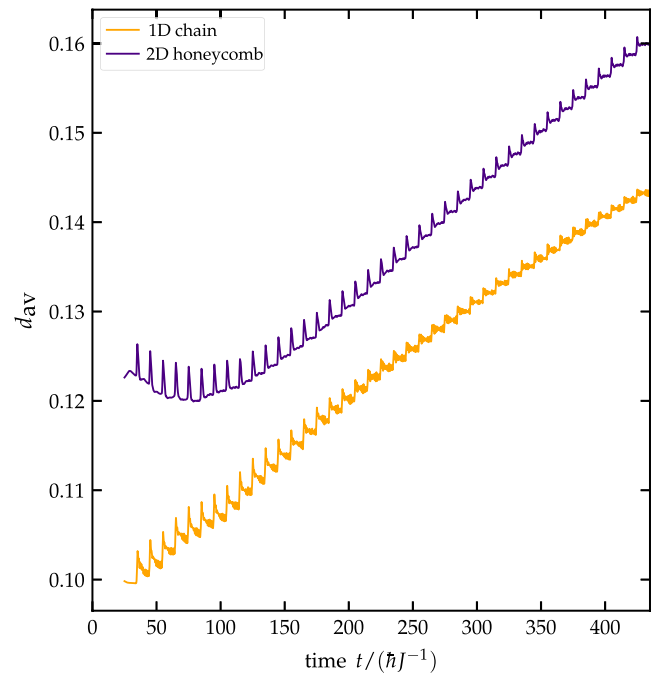


Figure 7. Cluster-averaged double occupation dynamics for the 2D honeycomb lattice (purple) and the 1D chain (orange). Both systems contain $L = 96$ sites and are excited 40 times. The Gaussian potential was used to mimic the projectile, and the input parameters match those of Figure 6.

same number of sites, $L = 96$. The figure confirms that the broad global minimum of $d_{av}(t)$ does not appear in a linear chain (orange curve), but is restricted to higher dimensionality. Interestingly, this effect is observed for the full Coulomb interaction and for the Gaussian model case but only if the system is sufficiently large, cf. Figure 5. Even though a simple explanation of this minimum is missing at the moment, we conclude that it is due to propagation and resonance effects of the electronic excitations that are triggered by the ion.

Furthermore, the initial double occupation of the honeycomb lattice is significantly larger than the corresponding value of the chain setup and the increase of $d_{av}(t)$ is faster. This is explained by the increased number of nearest neighbors of a lattice site, which supports the buildup of correlations.

3.4. Dependence of Doublon Creation on the Time Interval between Impacts

We now vary the frequency of ion impacts in a broad range. The results are shown in **Figure 8** for the largest honeycomb cluster ($L = 96$) using the Coulomb potential.

The upper panel illustrates how the total energy of the lattice evolves with the number of excitations for the respective impact frequencies. All calculations have been performed for the same total time duration, $t_{\max} = 650t_0$. For this reason, the total energy is much lower for high impact frequencies (green), since there are up to 20 times as many excitations compared to the low frequency case, where the potentials superpose each other. The flattening of the ion-impact peaks in the energy can also be

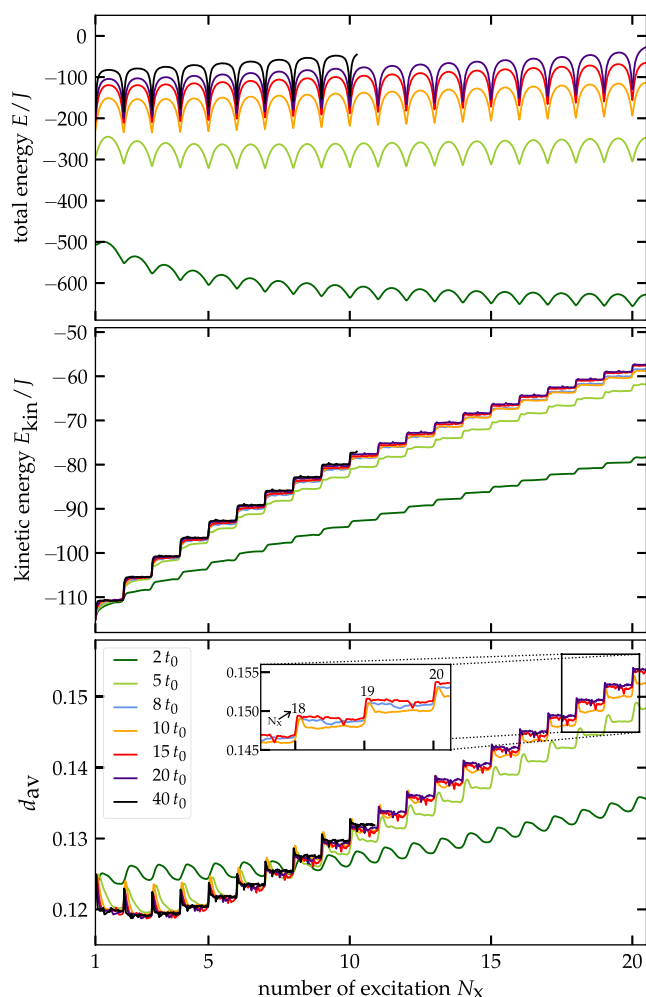


Figure 8. Dependence of total energy E (top figure) and average double occupation d_{av} (bottom figure) on the number of excitations N_x and the time interval between them, for a 96 sites honeycomb cluster. The six different colors denote different time intervals, Δt_{imp} , in between two consecutive excitations. The orange line ($10t_0$) corresponds to the interval used in all calculations provided earlier. The initial position and velocities of the projectiles match those introduced in Section 3.2.

attributed to that superposition, since the interim energy loss of the system directly induced through an impact becomes less relevant with every additional long-range Coulomb potential applied to the lattice electrons. To see the direct influence of the frequency variation, we consider the more sensitive kinetic energy (cf. Equation (20)) in the middle panel of Figure 8. Here, we see a similar buildup behavior for most time intervals Δt_{imp} , except for the highest ion frequencies, where the energy growth is hampered. For these cases, the ion frequency is on a similar time scale to the immediate electron dynamics in the target. Therefore, the finite correlation spreading and carrier mobility prevent a faster energy transfer.

This effect becomes even clearer for the double occupation (cf. bottom panel of Figure 8). Again, we observe that for sufficiently large Δt_{imp} , the successive double-occupation buildups coincide, whereas higher frequencies result in a decreased influence per

projectile. A peculiarity is found for $\Delta t_{imp} = 10t_0$ (orange curve), for which d_{av} lies slightly below the respective curves for $\Delta t_{imp} = 8t_0$ (blue) and $\Delta t_{imp} = 15t_0$ (red), see the inset of Figure 8. This non-monotonic behavior can be attributed to an interference of the impact frequency with one of the system's characteristic frequencies and will be further explained in context of Figure 9.

Another interesting observation is that the broad global minimum of d_{av} vanishes for very high frequencies. This indicates that the effect is caused by electronic correlation effects on longer time scales. To further investigate the non-monotonic effect in the double occupation, we now focus on the noise in-between two excitations and the vibration of d_{av} . In Figure 9, the time evolution of the average double occupation is shown for different impact frequencies.

Obviously, higher frequencies lead to a faster increase of the double occupation, due to the larger number of excitations. Note that there is a feature observed for all impact frequencies: a small kink in d_{av} (upward for early times and downward for later times) appears at approximately $10t_0$ after each projectile impact. This indicates that there exists a characteristic frequency in the $L = 96$ honeycomb cluster. For $\Delta t_{imp} = 10t_0$ (orange), this frequency coincides with the one of the ion impacts. This explains the unusual behavior of the double occupation for this case: instead of the small local minima, here maxima are observed.

To find an explanation for the mentioned characteristic frequency of the system, we now investigate the space-resolved carrier redistribution in the lattice.

3.5. Space-Resolved Electron Dynamics

The highly symmetric 96-site honeycomb cluster consists of four layers of hexagons. To increase the space resolution, we instead consider seven rings of sites, (sites on the n th ring are those that can be reached from the innermost ring within $n - 1$ steps), cf. Figure 1. In Figure 10, we show the time evolution of the average electron density (top) and double occupation (bottom) within each of these rings, following a single ion excitation through the center of the system.

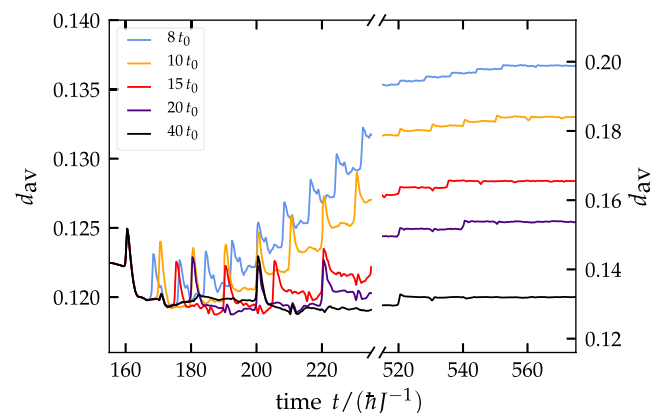


Figure 9. Cluster-averaged double occupation, as shown in Figure 8, but now plotted versus time. In the right part, the final stage of the time evolution around the final impact is displayed (note the break of the x-axis).

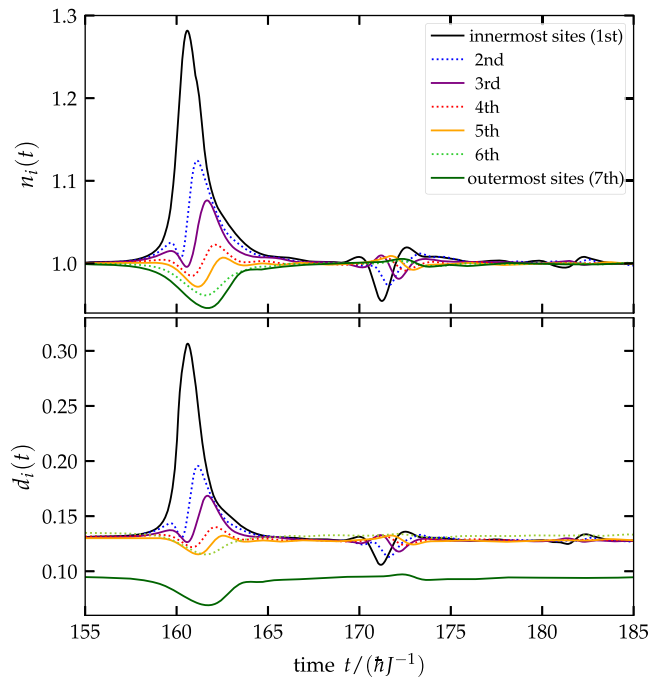
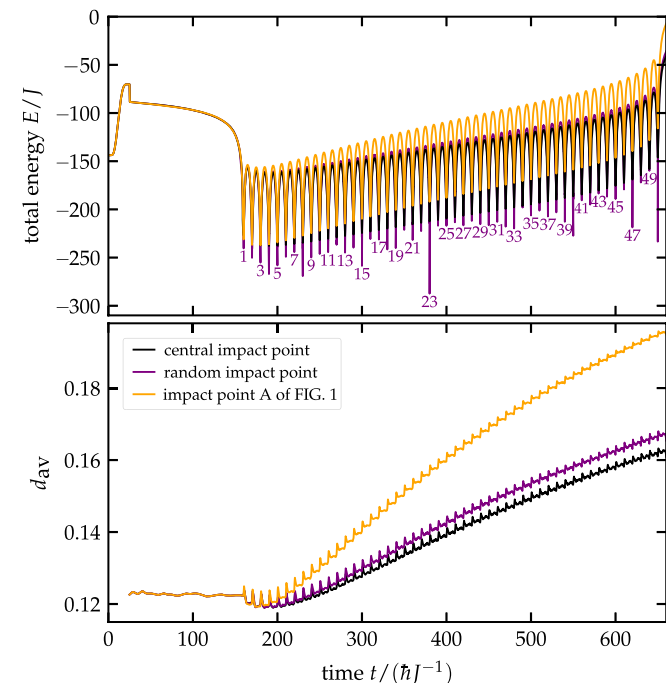


Figure 10. Time evolution of the local density (top) and double occupation (bottom) on the different honeycomb rings for an ion impact in the center. Due to the highly symmetric setup, the results coincide for all lattice sites of a single ring.

We observe a drastic initial increase in the density on the innermost ring that follows from the direct Coulomb attraction



by the charged projectile. Simultaneously, the outer rings are slightly depopulated as the electrons move toward the center. Subsequently, we observe a propagating density wave with a finite velocity through the honeycomb rings. For the outer rings, the density change becomes less pronounced, as the electrons spread across a larger number of lattice sites. After a short relaxation phase, the local densities exhibit a second peak (with lower amplitude and opposite sign), although the ion is already far away from the target and no additional excitation is invoked. Thus, the oscillation revival is caused by an intrinsic property of the finite cluster. The time interval between these events is approximately $\Delta t = 10t_0$, which agrees perfectly with the observed time delay of the energy kinks in Figure 9. Note that a second, less pronounced revival is observed after additional $10t_0$ (cf. the black curve in Figure 10).

The double occupation (bottom of Figure 10) exhibits a similar behavior as the density which is explained by the mean-field contribution to the doublon number. Note that for the outermost sites, we see a significantly lower double occupation—a property that is already present in the ground state and at the initial time, due to the reduced connectivity on the edges of the system.

3.6. Localized versus Random Impacts

We now consider a different setup, where the impact point of the projectiles is varied. To this end, we generate uniformly distributed positions within a circle of radius $1a_0$. For a fixed time interval of $\Delta t_{\text{imp}} = 10t_0$, we simulate successive ions of the same energy (cf. Equation (21)) penetrating through those randomized impact points. All computations are performed with a number of $N_x = 50$

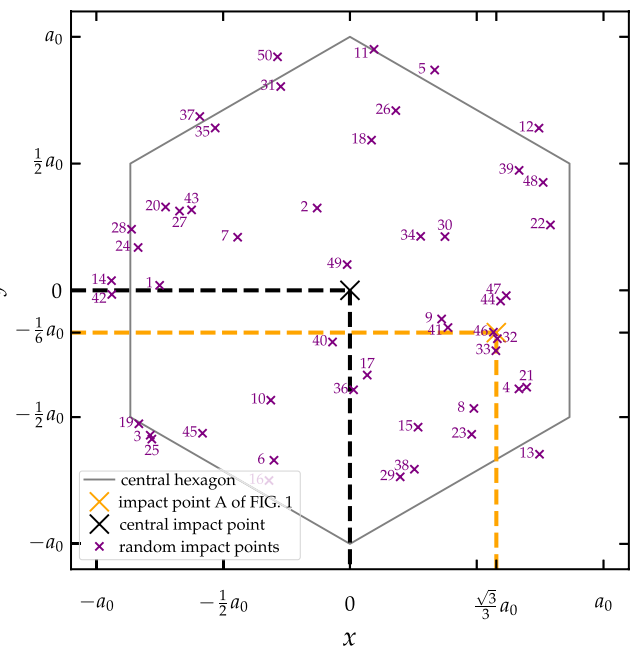


Figure 11. Response of a 96 site lattice to 50 excitations for three different selections of impact points (sketched in the right figure): black line: central impact; yellow: fixed impact point as in Figure 1; purple: random impact points, uniformly distributed within a radius of $1a_0$. **Top left:** time evolution of total energy of the lattice E and **bottom left:** time evolution of average double occupation d_{av} —the realized 50 impact points shown in the right panel are numbered in chronological order. The projectiles' initial velocity is the same as in Figure 3.

excitations. The results are presented in **Figure 11** for the total energy of the lattice (top), the cluster-averaged double occupation (bottom), and the impact positions (right). As a visual aid, the innermost hexagon of the 96-site cluster is shown (grey lines). The impact-point distribution is illustrated (purple) alongside with point A in Figure 1 (orange) and the central position (black). The purple numbers indicate the order of the excitations. From the behavior of the lattice energy and of the double occupation, we conclude that the random impact scenario produces results that are very similar to previous findings. In fact, both quantities fall predominantly between the curves for the impact point A (orange) and the central impact (black). Thus, we conclude that the spatially uniform distribution of ion impacts does not significantly change the electronic behavior. A peculiar feature is the random fluctuation of the energy minima, which is caused by the varying distance of the projectile to the nearest lattice sites. At the same time, the average double occupation is not affected by these variations and exhibits the same monotonic trend as for the central impact point (black curve). Furthermore, we recover the broad global minimum, discussed in Section 3.3.

4. Conclusions

In summary, we have extended the analysis of electronic correlations—specifically, doublon formation initiated by ion impact—in small hexagonal graphene-type clusters which was presented in a recent Letter.^[39] There the scenario of multiple ions hitting the target in the same spot and at fixed time intervals was analyzed, using an NEGF analysis coupled to an Ehrenfest treatment of the ions. The large computational effort of NEGF simulations limited the parameter range that could be studied.

Here, we applied the recently derived G1–G2 scheme^[54,68] to this problem. The advantageous linear scaling of this approach with respect to simulation duration has allowed us to significantly extend the previous analysis to larger clusters, more impacts, and variation of both impact point and time interval between impacts. We confirmed that increasing the number of impacts allows one to further increase the mean doublon number in the cluster until it eventually approaches the mean-field limit of 0.25. When the system size is increased, the increase of the doublon number slows down due to sharing of the impact energy among a growing number of electrons. An interesting observation was that, in a 2D hexagonal arrangement of L lattice sites, the average doublon number increases significantly faster compared to a linear arrangement of the same number of sites.

Our fully time-dependent approach is able to resolve nonadiabatic processes in the electronic subsystems and effects beyond linear response. Nonadiabatic effects are particularly evident at small time intervals between subsequent impacts because the electronic system has not enough time to return to the ground state before the next impact occurs. This can be clearly seen in the behavior of the average double occupation of the electrons shown in Figure 8. While for large time intervals between projectiles, the first few impacts result in a global minimum in the double occupation, the situation changes when the time interval is reduced. For the interval $5t_0$, only after reaching the global minimum do subsequent impacts lead to a periodic but steady increase in

the number of doublons; for $2t_0$, this behavior is present from the very first impact and no such minimum can be observed.

When the number of ion impacts is increased further, the system approaches a stationary electronic state where the doublon number saturates and is uniformly distributed over the cluster. The existence of such a nonequilibrium stationary state was reported for small clusters in Ref. [39] and is here confirmed for larger clusters. Since, in the present model, the electronic system is isolated, the excess energy stored in the electronic system cannot be dissipated to the lattice or the environment, and no relaxation toward equilibrium is observed. Thus, an extension to longer time scales requires the inclusion of electron–phonon interaction or the coupling to the lattice dynamics, analogous to Born–Oppenheimer density functional theory.

We analyzed two protocols of ion impact that can be realized in various experimental setups. First, we studied a strictly periodic sequence of ions that hit the same lattice site; this can be realized with ion guns. Second, we studied a situation where the impact point of the ions is chosen randomly. This case is closer to a gas or a plasma. Interestingly, we observed that the result for the average doublon number is almost the same as in the case of a fixed impact point. In further studies one could add random sampling of the time interval between ions to properly reflect the ion velocity distribution in the gas or plasma. This will allow one to make quantitative predictions for the interaction of plasmas with solids, cf., for example, Ref. [74].

Additional questions that are of interest in the context of ion–solid interaction are inner-ionic processes such as ion neutralization,^[44] electronic excitations, and secondary electron emission, for example, Ref. [75]. Such processes have recently become accessible to accurate measurements for highly charged projectiles impacting graphene and other correlated 2D materials (see, for example, Refs. [76,77]) and are still lacking a full theoretical description. The present NEGF approach within the G1–G2 scheme provides the proper starting point for this problem as it allows one to resolve the full dynamics of electronic correlations. At the same time, the present Hubbard model needs to be extended to include additional bands.^[16]

Acknowledgements

We thank Karsten Balzer for helpful discussions.

Open Access funding enabled and organized by Projekt DEAL.

Conflict of Interest

The authors declare no conflict of interest.

Data Availability Statement

The data that support the findings of this study are available from the corresponding author upon reasonable request.

Keywords

doublon formation, honeycomb cluster, Hubbard model, nonequilibrium Green functions, stopping power

Received: October 6, 2021
Revised: January 21, 2022
Published online: February 26, 2022

- [1] P. Sigmund, *Particle Penetration and Radiation Effects: General Aspects and Stopping of Swift Point Charges*, Springer Series in Solid-State Sciences, Springer, Berlin, Heidelberg **2006**.
- [2] I. Nagy, B. Apagyi, *Phys. Rev. A* **1998**, 58, R1653.
- [3] J. M. Pitarke, R. H. Ritchie, P. M. Echenique, *Phys. Rev. B* **1995**, 52, 13883.
- [4] P. M. Echenique, R. M. Nieminen, J. C. Ashley, R. H. Ritchie, *Phys. Rev. A* **1986**, 33, 897.
- [5] T. Dornheim, J. Vorberger, M. Bonitz, *Phys. Rev. Lett.* **2020**, 125, 085001.
- [6] M. Quijada, A. G. Borisov, I. Nagy, R. D. Muiño, P. M. Echenique, *Phys. Rev. A* **2007**, 75, 042902.
- [7] M. A. Zeb, J. Kohanoff, D. Sánchez-Portal, A. Arnau, J. I. Juaristi, E. Artacho, *Phys. Rev. Lett.* **2012**, 108, 225504.
- [8] A. Schleife, Y. Kanai, A. A. Correa, *Phys. Rev. B* **2015**, 91, 014306.
- [9] A. Ojanperä, A. V. Krasheninnikov, M. Puska, *Phys. Rev. B* **2014**, 89, 035120.
- [10] S. Zhao, W. Kang, J. Xue, X. Zhang, P. Zhang, *J. Phys.: Condens. Matter* **2014**, 27, 025401.
- [11] S. Bubin, B. Wang, S. Pantelides, K. Varga, *Phys. Rev. B* **2012**, 85, 235435.
- [12] F. Mao, C. Zhang, C.-Z. Gao, J. Dai, F.-S. Zhang, *J. Phys.: Condens. Matter* **2014**, 26, 085402.
- [13] R. Ullah, F. Corsetti, D. Sánchez-Portal, E. Artacho, *Phys. Rev. B* **2015**, 91, 125203.
- [14] J. M. Pruneda, D. Sánchez-Portal, A. Arnau, J. I. Juaristi, E. Artacho, *Phys. Rev. Lett.* **2007**, 99, 235501.
- [15] M. A. Zeb, J. Kohanoff, D. Sánchez-Portal, E. Artacho, *Nucl. Instrum. Methods Phys. Res. B* **2013**, 303, 59 [Proceedings of the 11th Computer Simulation of Radiation Effects in Solids (COSIRES) Conference, Santa Fe, New Mexico, USA, July 24–29, 2012].
- [16] A. Kononov, A. Schleife, *Nano Lett.* **2021**, 21, 4816.
- [17] J. F. Ziegler, M. Ziegler, J. Biersack, *Nucl. Instrum. Methods Phys. Res. B* **2010**, 268, 1818 [19th International Conference on Ion Beam Analysis (IBA 2009), 7–11 September 2009, University of Cambridge, UK].
- [18] V. I. Anisimov, F. Aryasetiawan, A. I. Lichtenstein, *J. Phys.: Condens. Matter* **1997**, 9, 767.
- [19] R. Singla, G. Cotugno, S. Kaiser, M. Först, M. Mitrano, H. Y. Liu, A. Cartella, C. Manzoni, H. Okamoto, T. Hasegawa, S. R. Clark, D. Jaksch, A. Cavalleri, *Phys. Rev. Lett.* **2015**, 115, 187401.
- [20] L. Kadanoff, G. Baym, *Quantum Statistical Mechanics*, Benjamin, New York **1962**.
- [21] G. Stefanucci, R. van Leeuwen, *Nonequilibrium Many-Body Theory of Quantum Systems*, Cambridge University Press, Cambridge **2013**.
- [22] K. Balzer, M. Bonitz, *Nonequilibrium Green's Functions Approach to Inhomogeneous Systems*, Springer, Berlin, Heidelberg **2013**.
- [23] N. Schlünzen, S. Hermanns, M. Scharnke, M. Bonitz, *J. Phys.: Condens. Matter* **2020**, 32, 103001.
- [24] P. Danielewicz, *Ann. Phys.* **1984**, 152, 305.
- [25] H. S. Köhler, *Phys. Rev. C* **1995**, 51, 3232.
- [26] M. Bonitz, D. Kremp, D. C. Scott, R. Binder, W. D. Kraeft, H. S. Köhler, *J. Phys.: Condens. Matter* **1996**, 8, 6057.
- [27] N. H. Kwong, M. Bonitz, R. Binder, H. S. Köhler, *Phys. Status Solidi B* **1998**, 206, 197.
- [28] N.-H. Kwong, M. Bonitz, *Phys. Rev. Lett.* **2000**, 84, 1768.
- [29] R. Binder, S. Köhler, M. Bonitz, *Phys. Rev. B* **1997**, 55, 5110.
- [30] N. E. Dahlen, R. van Leeuwen, *J. Chem. Phys.* **2005**, 122, 164102.
- [31] P. Myöhänen, A. Stan, G. Stefanucci, R. van Leeuwen, *EPL (Europhys. Lett.)* **2008**, 84, 67001.
- [32] P. Myöhänen, A. Stan, G. Stefanucci, R. van Leeuwen, *Phys. Rev. B* **2009**, 80, 115107.
- [33] K. Balzer, M. Bonitz, R. van Leeuwen, A. Stan, N. E. Dahlen, *Phys. Rev. B* **2009**, 79, 245306.
- [34] N. Schlünzen, S. Hermanns, M. Bonitz, C. Verdozzi, *Phys. Rev. B* **2016**, 93, 035107.
- [35] N. Schlünzen, J.-P. Joost, F. Heidrich-Meisner, M. Bonitz, *Phys. Rev. B* **2017**, 95, 165139.
- [36] M. P. von Friesen, C. Verdozzi, C.-O. Almbladh, *Phys. Rev. Lett.* **2009**, 103, 176404.
- [37] S. Hermanns, N. Schlünzen, M. Bonitz, *Phys. Rev. B* **2014**, 90, 125111.
- [38] K. Balzer, N. Schlünzen, M. Bonitz, *Phys. Rev. B* **2016**, 94, 245118.
- [39] K. Balzer, M. R. Rasmussen, N. Schlünzen, J.-P. Joost, M. Bonitz, *Phys. Rev. Lett.* **2018**, 121, 267602.
- [40] M. Bonitz, K. Balzer, N. Schlünzen, M. Rasmussen, J.-P. Joost, *Phys. Status Solidi B* **2019**, 257, 1800490.
- [41] N. Schlünzen, K. Balzer, M. Bonitz, L. Deuchler, E. Pehlke, *Contrib. Plasma Phys.* **2019**, 59, 201800184.
- [42] F. Aumayr, A. El-Said, W. Meissl, *Nucl. Instrum. Methods Phys. Res. B* **2008**, 266, 2729 [Fourteenth International Conference on Radiation Effects in Insulators (REI-14), 28 August–1 September 2007, Caen, France].
- [43] E. Gruber, R. A. Wilhelm, R. Pétuya, V. Smejkal, R. Kozubek, A. Hierzenberger, B. C. Bayer, I. Aldazabal, A. K. Kazansky, F. Libisch, A. V. Krasheninnikov, M. Schleberger, S. Facsko, A. G. Borisov, A. Arnau, F. Aumayr, *Nat. Commun.* **2016**, 7, 13948.
- [44] K. Balzer, M. Bonitz, *Contrib. Plasma Phys.* **2021**, 61, 202100040.
- [45] N. E. Dahlen, R. van Leeuwen, *Phys. Rev. Lett.* **2007**, 98, 153004.
- [46] A. Stan, N. E. Dahlen, R. van Leeuwen, *J. Chem. Phys.* **2010**, 130, 224101.
- [47] K. Balzer, S. Bauch, M. Bonitz, *Phys. Rev. A* **2010**, 81, 022510.
- [48] K. Balzer, S. Bauch, M. Bonitz, *Phys. Rev. A* **2010**, 82, 033427.
- [49] M. Garny, M. M. Müller, in *High Performance Computing in Science and Engineering, Garching/Munich 2009* (Eds: S. Wagner, M. Steinmetz, A. Bode, M. M. Müller), Springer, Berlin, Heidelberg **2010**, pp. 463–474.
- [50] S. Latini, E. Perfetto, A.-M. Uimonen, R. van Leeuwen, G. Stefanucci, *Phys. Rev. B* **2014**, 89, 075306.
- [51] P. Lipavský, V. Špička, B. Velický, *Phys. Rev. B* **1986**, 34, 6933.
- [52] R. Tuovinen, R. van Leeuwen, E. Perfetto, G. Stefanucci, *J. Chem. Phys.* **2021**, 154, 094104.
- [53] E. Perfetto, A.-M. Uimonen, R. van Leeuwen, G. Stefanucci, *Phys. Rev. A* **2015**, 92, 033419.
- [54] N. Schlünzen, J.-P. Joost, M. Bonitz, *Phys. Rev. Lett.* **2020**, 124, 076601.
- [55] D. Karlsson, R. van Leeuwen, Y. Pavlyukh, E. Perfetto, G. Stefanucci, *Phys. Rev. Lett.* **2021**, 127, 036402.
- [56] Y. Pavlyukh, E. Perfetto, G. Stefanucci, *Phys. Rev. B* **2021**, 104, 035124.
- [57] M. I. Katsnelson, *Graphene: Carbon in Two Dimensions*, Cambridge University Press, Cambridge **2012**.
- [58] S. Mishra, D. Beyer, K. Eimre, S. Kezilebieke, R. Berger, O. Gröning, C. A. Pignedoli, K. Müllen, P. Liljeroth, P. Ruffieux, X. Feng, R. Fasel, *Nat. Nanotechnol.* **2020**, 15, 22.
- [59] S. Mishra, X. Yao, Q. Chen, K. Eimre, O. Gröning, R. Ortiz, M. Di Giovannantonio, J. C. Sancho-García, J. Fernández-Rossier, C. A. Pignedoli, K. Müllen, P. Ruffieux, A. Narita, R. Fasel, *Nat. Chem.* **2021**, 13, 581.
- [60] J. Li, S. Sanz, N. Merino-Díez, M. Vilas-Varela, A. Garcia-Lekue, M. Corso, D. G. de Oteyza, T. Frederiksen, D. Peña, J. I. Pascual, *Nat. Commun.* **2021**, 12, 5538.

- [61] M. Schüler, M. Rösner, T. O. Wehling, A. I. Lichtenstein, M. I. Katsnelson, *Phys. Rev. Lett.* **2013**, *111*, 036601.
- [62] J.-P. Joost, N. Schlünzen, M. Bonitz, *Phys. Status Solidi B* **2019**, *257*, 1800498.
- [63] J.-P. Joost, A.-P. Jauho, M. Bonitz, *Nano Lett.* **2019**, *19*, 9045.
- [64] S. Scherg, T. Kohlert, J. Herbrych, J. Stolpp, P. Bordia, U. Schneider, F. Heidrich-Meisner, I. Bloch, M. Aidelsburger, *Phys. Rev. Lett.* **2019**, *121*, 130402.
- [65] C. Gross, I. Bloch, *Science* **2017**, *357*, 995.
- [66] L. Keldysh, *Sov. Phys. JETP* **1965**, *20*, 1018 [*Zh. Eksp. Teor. Fiz.* **1964**, *47*, 1515].
- [67] N. Schlünzen, M. Bonitz, *Contrib. Plasma Phys.* **2016**, *56*, 5.
- [68] J.-P. Joost, N. Schlünzen, M. Bonitz, *Phys. Rev. B* **2020**, *101*, 245101.
- [69] M. Bonitz, *Quantum Kinetic Theory*, 2nd ed., Springer, Cham, Switzerland **2016**.
- [70] S. Hermanns, K. Balzer, M. Bonitz, *Phys. Scr.* **2012**, *2012*, 014036.
- [71] K. Balzer, S. Hermanns, M. Bonitz, *J. Phys.: Conf. Ser.* **2013**, *427*, 012006.
- [72] J.-P. Joost, N. Schlünzen, M. Bonitz, in preparation.
- [73] L. Borkowski, Bachelor thesis, Christian-Albrechts-Universität zu Kiel, **2021**.
- [74] M. Bonitz, A. Filinov, J.-W. Abraham, K. Balzer, H. Kählert, E. Pehlke, F. X. Bronold, M. Pamperin, M. Becker, D. Loffhagen, H. Fehske, *Front. Chem. Sci. Eng.* **2019**, *13*, 201.
- [75] M. Pamperin, F. X. Bronold, H. Fehske, *Phys. Rev. B* **2015**, *91*, 035440.
- [76] R. A. Wilhelm, E. Gruber, J. Schwestka, R. Kozubek, T. I. Madeira, J. P. Marques, J. Kobus, A. V. Krasheninnikov, M. Schleberger, F. Aumayr, *Phys. Rev. Lett.* **2017**, *119*, 103401.
- [77] A. Niggas, S. Creutzburg, J. Schwestka, B. Wöckinger, T. Gupta, P. Grande, D. Eder, J. Marques, B. Bayer, F. Aumayr, R. Bennett, R. Wilhelm, *Commun. Phys.* **2021**, *4*, 180.